

## N O T I C E

THIS DOCUMENT HAS BEEN REPRODUCED FROM  
MICROFICHE. ALTHOUGH IT IS RECOGNIZED THAT  
CERTAIN PORTIONS ARE ILLEGIBLE, IT IS BEING RELEASED  
IN THE INTEREST OF MAKING AVAILABLE AS MUCH  
INFORMATION AS POSSIBLE

Carnegie Institution of  
Washington, D.C.

NAG 8-357  
~~NAG 8-357~~  
NSF 83-51447

X-rays from the Radio Halo of Virgo A = M87

Results



(NASA-CR-176303) X-RAYS FROM THE RADIO HALO  
OF VIRGO A = M87 (Carnegie Institution of  
Washington) 43 P HC A03/MF A01 CSCL 03B

N86-13285

Unclas  
G3/93 27652

## I INTRODUCTION

The inverse Compton (IC) process occurs when low frequency photons are scattered to higher frequencies by relativistic electrons of Lorentz factor  $\gamma$ , with an energy boost of  $\sim \gamma^2$ . The lobes and jets of radio galaxies contain huge reservoirs of synchrotron emitting electron with  $\sim 10^2 - 10^4$ . It is thus expected that they will scatter microwave background photons with  $\nu \sim 10^{11}$  Hz into the X-ray band where they would be seen by satellite borne X-ray detectors. Despite the obligatory nature of this process, there has not been a single confirmed detection of X-ray IC emission from extended extragalactic radio structures. The most likely case prior to the launch of the Einstein Observatory, a report of X-ray emission from the outer lobes of Centaurus A from the Ariel V satellite (Cooke et al. 1978), was shown by SAS-3 researchers to be due to confusion by an unrelated X-ray source (Marshall and Clark 1981). Although a few jets and lobes appear to have X-ray counterparts in Einstein images (e.g., Feigelson et al. 1981; Harris et al. 1984; Burns et al. 1985; see reviews by Feigelson 1983 and 1985), they can not be confidently attributed to IC processes. The bright X-ray jet knots of Cen A and Vir A, in particular, are most likely due to direct synchrotron from extremely energetic electrons (Schreier et al, 1982; Burns et al. 1983).

This general failure to detect IC X-rays appears to be due to a conspiracy of numerical factors. Given the estimated magnetic field strengths of  $B_{eq} \sim 10^{-6} - 10^{-4}$  G and the microwave background photon

density  $U_{ph} \sim 10^{-13}$  erg cm $^{-3}$ , typical radio components with  $S_{\nu} < 100$  Jy at 100 MHz will produce X-ray flux densities  $< 0.001 - 0.0001$   $\mu$ Jy, which is below the sensitivity limits of current X-ray instrumentation (Harris and Grindlay 1979). Only unusually strong radio sources with unusually weak magnetic fields should be detectable. Current upper limits on IC X-rays generally provide only uninteresting limits on the field strength (Feigelson and Berg 1983), with a few exceptions such as the Cen A outer lobes limit (Marshall and Clark 1981). A single confirmed detection of IC would be highly significant, as it would determine whether the many assumptions implied by the use of equipartition between the magnetic field and electron pressures (e.g. Miley 1980) are in fact valid. These include assumptions regarding the pressure of relativistic protons, the filling factor, the orientation of the magnetic field, and the source geometry.

A number of researchers (Turland 1975; Andernach et al. 1979; Dennison 1980) have noted that the radio halo of Virgo A = 3C274 = M87 provides an excellent opportunity to detect IC X-rays because of its high flux ( $S_{\nu} = 1360$  Jy at 101 MHz) and low equipartition field strength ( $B_{eq} = 4 - 8$   $\mu$ G). The predicted IC flux would be of order 10% of the thermal emission from the dense 'cooling flow' of intracluster gas that is responsible for most of the X-ray emission of M87 (e.g. Fabricant et al. 1980; Stewart et al. 1984). It might be resolved from the thermal component because of the distinctive morphology of the radio halo: two misaligned lobes 2' to 6' east and south-west of the nucleus (Andernach et al. 1979; Kotanyi 1980).

When the Einstein High Resolution Imager (HRI) obtained a deep exposure of M87, an X-ray component with just this morphology was seen superposed on the large-scale thermal component (Schreier et al. 1982, henceforth SGF). The observed excess of  $\sim 0.02$  HRI cts  $s^{-1}$  was within a factor of two of the predicted IC level, and thus represents the best case to date for X-ray IC emission from an extended radio structure.

The purpose of this study is to investigate in more detail the associated X-ray and radio emission in the Virgo A halo discovered by SGF. Improved Einstein HRI data and new radio maps obtained with the Very Large Array are described (section II), and the relation between the X-ray and radio structures is carefully examined (section III). Section IV presents several possible explanations for the X-ray emission. The IC model is found to be viable only if the magnetic field is variable and substantially weaker than the equipartition value. The principal alternative is excess thermal X-rays due to compression of the intracluster medium by the radio lobe. In either case, the association of such prominent radio and X-ray structures is unique among known radio galaxies.

## II Observations and Data Analysis

### (a) X-ray Observations

The study by SGF was based on a 75,600 s exposure of M87 obtained on July 5 1979 with the Einstein HRI. The instrument is

described by Giacconi et al. (1979). We have added to this image a second exposure of duration 51,200 s obtained on December 9 1980. Both data sets were reprocessed with improved aspect solutions (Rev. 1.0), and data acquired when the star trackers were out of LOCK mode were rejected. The resultant merged image contains 74,465 s effective exposure and should be free of aspect errors greater than 1-2 arc seconds. The HRI is not subject to any other temporal or spatial anomaly; detector background is ignored because it is nearly uniform and will be removed in the analysis of asymmetric emission.

As described by SGF, the image shows four X-ray components: a cusp or point source associated with the active nucleus; a bright region from the radio/optical synchrotron jet 10"-20" west of the nucleus; diffuse emission extending beyond the 35' HRI field corresponding to the dense thermal gas; and the asymmetric excess around 3' - 5' east and south-west of the nucleus associated with the radio halo. Figure 1a shows a contour map of the merged HRI image after smoothing with a 20" FWHM Gaussian. The slightly triangular contours are the only sign of the asymmetric component in this representation.

The main task in further revealing the structure of the asymmetric component associated with the radio halo is to remove the thermal gas component. Though in principle one could subtract a theoretical model of the gaseous emission based on other X-ray data and a model of the gravitational potential, in practice researchers have assumed the X-rays are entirely thermal in origin and have used

them to derive the mass distribution (e.g. Fabricant et al. 1980; Stewart et al. 1984). Since there is no adequate independent knowledge of the mass distribution, we have made the a priori assumption that the thermal component contributes all of the spherically symmetric HRI counts, with the additional condition that its radial distribution monotonically decrease with distance from the nucleus. Any residual asymmetric emission is then compared to the radio structure. There is no guarantee that the gaseous component is truly symmetric (indeed, we attribute at least some to the asymmetry to it; see Appendix A), or that the symmetric component does not include some non-thermal emission. Despite these limitations, the separation between symmetric and asymmetric components suffers little operational ambiguity.

To obtain a map of the asymmetric X-ray component, the HRI image was binned into 4" pixels and divided into azimuthal octants and differentially spaced annuli centered on the nucleus. The inner 40" with the jet and steeply rising core region were ignored. The octant in each annulus with the lowest surface brightness was chosen to represent the symmetric component at that radius. The lowest octants generally occurred with P. A. 0 - 90d. The resulting surface brightness distribution follows closely the lowest curves shown in Figure 3 of SGF. Using parabolic interpolation between the annuli, the symmetric surface brightness was evaluated and subtracted from each pixel in the map. Figure 1b shows the residual map after smoothing with a 15" FWHM Gaussian.

Conversion from HRI cts  $s^{-1}$  to physical units is quite uncertain given the lack of energy discrimination in the HRI and the unknown spectral characteristics of the asymmetric component. We have adopted a spectrum expected if the emission is truly IC: a power law with energy index  $\alpha = 1.0$  (taken from the radio spectrum around 100-400 MHz; Andernach et al. 1979) and a galactic absorption of  $N_H = 4 \times 10^{20} \text{ cm}^{-2}$ . The conversion factors between 1 HRI count/1000 seconds and physical units are then (Harris 1984)  $1 \text{ ct}/1000 \text{ s} = 0.016 \text{ } \mu\text{Jy}$  (evaluated at 1 keV) and  $1 \text{ ct}/1000 \text{ s} = 2.9 \times 10^{39} \text{ erg s}^{-1}$  (assuming a distance of 16 Mpc). If the emission process is thermal bremsstrahlung from gas with cosmic abundances at  $T = 2 \times 10^7 \text{ K}$ , which is the estimated temperature for gas several arc minutes from the nucleus (Stewart et al. 1984), the flux density and luminosity conversion factors would be 5.7 and 1.2 times higher respectively. The flux density is thus extremely sensitive to the unknown spectral index of the asymmetrical component, though the broad band flux and luminosity is not. We thus caution that, while the residual map shown in Figure 1b is an accurate representation of the observed asymmetric X-ray emission, the associated flux density map might differ significantly due to spectral variations.

#### (b) Radio Observations

Given the excellent X-ray residual map with resolution of  $15''$  or better, we sought to obtain a radio map of the Vir A halo with similar resolution. This is extremely difficult because the halo has a very low surface brightness and surrounds a very bright core. (The



core component is itself complex with a VLBI source at the nucleus, the one-sided jet, and two inner lobes.) There is an unavoidable tradeoff between resolution and dynamic range; dynamic ranges of  $10^3$  -  $10^4$  are needed at sub-arcminute resolution. The effort is further complicated by the large angular size of the halo (around  $15'$ ) which can be overresolved by widely spaced interferometers and can exceed the primary beam widths of some telescopes. Observations of the halo are best done at low frequencies where its flux density exceeds that of the core component.

There have been three efforts to map the two-dimensional structure of the halo, which was discovered by Mills (1952) in an early interferometric experiment at 101 MHz. A crude interferometric map with  $3' \times 4'$  resolution was made by Cameron (1971) at 408 MHz with the Molonglo Cross. Andernach et al. (1979) obtained a 4.8 GHz map with  $2.6'$  resolution and a 10.7 GHz map with  $75''$  resolution with the single Bonn 100-m telescope. The latter shows few details because of the low halo flux at this high frequency. Lastly, Kotanyi (1980) made a 610 MHz map with  $4.3' \times 0.9'$  resolution with the Westerbork interferometer. The elongated beam is due to the absence of north-south baselines. Polarization maps were also obtained from the Bonn and WRST data.

The NRAO Very Large Array (VLA) in its low resolution configurations should provide an improved view of the halo. The instrument is described by Thompson et al. (1980). Three data sets were available for investigation: (1) A full synthesis at 1.4 GHz,

interspersed with snapshots at 5 GHz, obtained on January 30 1982 with a hybrid C/A configuration (north arm extended); (2) full syntheses at 1.4 and 5 GHz obtained on April 6 1984 with the standard C configuration; and (3) a series of snapshots spanning 6 hours with 1 hour net exposure at 1.4 GHz and 5 GHz respectively obtained on June 2 1983 in the D configuration. The second data set was a byproduct of an intercontinental VLBI observation of the Vir A nucleus (see Reid et al. 1982 for an earlier epoch of this experiment). The third data set was part of an effort to map the calibrator sources of Baars et al. (1977), and was kindly made available by Dr. R. Perley. The antenna phases and gains were calibrated for each data set using standard VLA procedures. Flux densities were bootstrapped to 3C286. Maps were made for each database using a variety of tapering and weighting functions, after which there were CLEANed. The visibility data were then self-calibrated to a model based on the clean components.

The difficulties of mapping the halo at high resolution were rapidly encountered. The 1.4 GHz C/A hybrid and C configuration maps, with synthesized beamwidths between 5" and 30" depending on the tapering function, could not be adequately cleaned or self-calibrated. Dynamic ranges reached 1000:1 (Peak flux density: RMS noise) but the low halo surface brightness at these high resolutions requires dynamic ranges several times higher to see details. Furthermore, only ~70% of the 200 Jy in the source appears in the cleaned map because much of the halo flux occurs on very low spatial frequencies. It is resolved out in the C configuration with

a minimum baseline of 315 wavelengths. Insertion of a large zero-spacing flux does not improve map quality, probably because of the non-uniform structure of the large scale emission.

The only acceptable 1.4 GHz maps were obtained with the D configuration with a minimum baseline of 200 wavelengths. The data were subjected to four passes of cleaning and self-calibration, in which phases only were adjusted. The recovered flux density is 197 Jy which is consistent with the total  $209 \pm 9$  Jy in the source at 1.465 GHz (Baars et al. 1977). Figures 2a and 2b show two representations of the resultant total intensity map. The first is subjected to a Gaussian taper at 1500 wavelengths and has a synthesized beam width of 72" FWHM. The second is untapered with 'super-uniform' weighting in the UV plane (see Sramek 1983) to give a high resolution of 39" FWHM. The dynamic ranges of the maps are 1300:1 and 3400:1 respectively. The polarization properties are shown in Figures 2a and 2b as electric field vectors proportional in length to the polarization fraction at each location.

In addition to the 1.4 GHz maps, the 5 GHz data were also examined. The three-fold higher resolution, lower halo flux and smaller VLA primary beam (9' FWHM at 5 GHz) all conspire against retrieval of the more extended parts of the halo. Most the 5 GHz data sets failed to show more than 10% of the estimated 16 Jy in the halo (Andernach et al. 1979) due to the missing short baselines. Nonetheless, we show the best obtained map, from the C configuration data tapered at 3000 wavelengths, in Figure 3. It has a 40"

synthesized beamwidth and shows a dynamic range of  $\sim 3000:1$ . A significant primary beam attenuation correction factor has been applied. No polarization data is available because the array was phased for the VLBI experiment. We emphasize that, because of the missing flux, the brightness of the features in Figure 3 should not be used for quantitative measures of flux or spectral indices.

### III Results

#### (a) X-ray and Radio Morphologies

The asymmetrical X-ray emission appears on two spatial scales in Figure 1b: the bright emission within  $5'$  of the nucleus associated with the radio halo; and a low surface brightness excess seen out to  $\sim 10'$  from the nucleus to the NW and SE. The latter is seen in the contour map as a sprinkling of low level contours, and is quite apparent on displays at lower resolution. Unrelated to the radio source, this X-ray structure is probably associated with an eccentricity in optical isophotes seen in M87. Since this diverges from the principal topic of this paper, we discuss it briefly in Appendix A.

The X-ray component associated with the radio halo might be described as a triangular region with the nucleus at one vertex and two adjacent arms oriented along P.A.  $90^\circ$  ( $4'$  long) and P.A.  $225^\circ$  ( $5'$  long). The region between the arms is smoothly filled, with a surface brightness 50-80% that of the arms. The eastern arm is

brightest 2.0' from the nucleus. Its width at this point is 1.3' FWHM and 2.5' FWZI. The arm dims and tapers to the east, ending at a resolved spot 1.0' FWHM centered 4.1' from the nucleus along P.A. 93°. The southwestern arm also peaks 1.8' from the nucleus, but has a somewhat different transverse brightness distribution. The north side of the structure is quite straight and sharp with 0.3' HWHM, while the south side declines more gradually with 1.5' HWHM. The sharp edge of this arm is visually quite evident even in the original HRI image dominated by the symmetrical thermal component.

A matter not fully resolved is whether the X-ray asymmetries extend directly into the nucleus. Pixel digitization and the steep gradient of the subtracted symmetric component hinder detailed analysis. Nonetheless, it appears that the eastern arm may extend directly into the central 20" along P.A. 110°, while the southwestern arm appears to start about 40" from the nucleus.

The radio structure shown in Figures 2a and 2b reveal considerably more detail than earlier maps of the halo. The total extent of the source is 13' elongated along approximately P.A. 45°. But, unlike most double sources the interior features are generally not aligned along this axis. The principal features might be described as follows (in order of increasing distance from the nucleus): (a) an unresolved knot 2.1' west of the nucleus along P.A. 265°; (b) an amorphous component to the east centered 3.0' from the nucleus along P.A. 85°, 2.5' FWHM in size; (c) a jet-like component extending 2' to 5' southwest of the nucleus along P.A. 45°, with

width 1.6' FWHM transverse of the axis; and (c) the large-scale envelope mentioned above. It is not clear these features are truly independent of each other. The higher resolution maps at 1.4 and 5 GHz (Figures 2b and 3) distinctly suggest that emitting material flows through the western knot into the southwest feature as a continuous, knotty jet. The southwest jet fades smoothly into the large-scale envelope, though the latter is present on the northeast side of the source where no jet is seen.

The polarization structure of the halo is even more unusual. Though ~40% of the unpolarized halo flux lies east and north of the nucleus, less than 5% of the polarized flux lies in these directions. Virtually all of the polarized emission is concentrated at the far end of the southwest jet. Its principal component is a ridge 4' in length oriented along P.A. 135°, or transverse to the axis of the unpolarized emission. Yet, the direction of the magnetic field appears generally parallel to the unpolarized axis, which is contrary to the orientation generally seen in low luminosity radio jets (Bridle 1984). Some weak polarized emission is seen near (but not coincident with) the west knot, again with a field orientation suggesting a flow from the knot into the southwest jet. All interpretation of the magnetic field orientations is somewhat speculative, as the importance of Faraday rotation at 1.4 GHz has not been established.

In Appendix B we discuss the halo radio morphology in light of current models of radio galaxy structure. We find the halo can

probably be classified as a wide-angle tail (WAT) source. Its structure might be attributed to a rotating nucleus, but more likely to bent jets seen in projection. Further study, particularly multi-frequency polarization maps to elucidate the Faraday effects, is warranted.

The descriptions given above indicate that the morphologies of the halo at the two wavebands are similar but not identical. The resemblances lie in the principal axes of emission, east and southwest of the nucleus, and the overall extent of the emission. Differences include the brightness profiles along the principal axes, (e.g., the X-ray emission peaks closer to the nucleus than the radio emission), and radio structures that do not appear in the X-ray map (e.g. the western knot and large-scale envelope to the north). The radio map resolution is not high enough to say whether or not radio emission is absent to the southeast of the nucleus where the prominent X-ray bridge appears. The only case of directly coincident features at the two wavebands are the east radio peak and the faint X-ray spot at the end of the eastern X-ray arm.

#### (b) Quantitative Comparison of the X-ray and Radio Maps

We first consider the halo structures as a whole. Within the lowest contour of Figures 1b and 1c, the HRI residual image shows about 10,300 counts or 138 cts/1000 s in a 19 square arc minute region. This value is accurate to about 10%, and excludes the inner 40" core region. This count rate of the asymmetrical component

comprises about 25% of the count rate seen in the original HRI image (Figure 1a). It is more than 3 times higher than the 40 cts/1000 s estimated by SGF from a less detailed analysis because they considered only a limited range of radii (2' to 5') and position angles (90° - 120° and 210° - 240°). Using the conversions given in section IIa, this count rate corresponds to a 0.2-4 keV luminosity of  $4.0 \times 10^{41}$  ergs s<sup>-1</sup> (accurate to 20% except for possible distance uncertainties) and a 1 keV flux density of 2.2  $\mu$ Jy (which may be inaccurate by a factor of 5 due to spectral uncertainties).

Within the lowest contour of Figures 2a and 2b, the 1.4 GHz radio flux density is 197 Jy of which 58 Jy lies outside the central core region. The separation of the core from the halo is not clearcut; Andernach et al. (1979) show that a decomposition of 120 Jy in the core and 80 Jy in the halo give more consistent 0.1-10 GHz spectra for both components. Assuming the latter value, then the X-ray/radio flux density ratio  $\log[S(1\text{keV})/S(1.4\text{ GHz})] = -7.56$  corresponding to a spectral index

$$\alpha_{\text{rx}} = -0.92.$$

As discussed in the previous section, the relative radio/X-ray emission is highly variable across the source. Figure 4 shows a superposition of the 39" resolution radio and X-ray residual maps with eight locations marked that show a range of different properties. Table 1 gives the measured radio flux density, polarization fraction, HRI counts/39" beam, estimated X-ray flux density, X-ray/radio flux density ratio and spectral index for each



location. The results may be summarized as follows. The radio surface brightness ranges over a factor of 5 and the polarization fraction varies between 28% and <1% (three-sigma limit). The X-ray surface brightness ranges over a factor of >7. The X-ray/radio ratio varies by a factor >10 across the halo, with a spectral index of approximately  $\alpha_{\text{rx}} = -0.9$  to  $-1.0$ .

#### IV DISCUSSION

Before considering the possible explanations for the associated, but not entirely coincident, X-ray and radio structures in Vir A, we briefly compare it to other sources. In both wavebands, the structure is remarkably bright. In X-rays, its HRI count rate is 5 times greater than the jet in Vir A (SGF), 20 times greater than the jet in Cen A (Feigelson et al. 1981), 70 times greater than the jet in 3C273 (Willingale 1981), and an order of magnitude brighter than possible X-ray counterparts of radio structures in other galaxies (Harris et al. 1984; Burns et al. 1985). Its soft X-ray flux is sufficient to have been detected in the UHURU, Ariel V and HEAO-1 all-sky surveys even without the presence of the dominant symmetric component. In radio, the Vir A halo is the third brightest extragalactic radio source at 178 MHz. Yet, if M87 lay at a distance of 500 Mpc ( $z = 0.10 - 0.15$ ) rather than 15 Mpc, only 5-10 counts would have appeared in a long HRI exposure and the X-ray source would be only marginally detectable. At that distance, its 1.4 GHz radio flux density would be 80 mJy. Since there are large numbers of such weak distant radio galaxies, it seems quite likely that many similar X-ray structures are present at levels below that detectable with the

## Einstein Observatory.

## (a) Inverse Compton (IC) Emission

As discussed in section I, the radio halo's relativistic electrons must scatter photons of the microwave background into the X-ray band. The ratio of IC to synchrotron flux density from this process, assuming a background blackbody spectrum with  $T = 2.7^\circ\text{K}$  and ignoring negligible redshift factors, is (Harris and Grindlay 1979)

$$\log(S_x/S_v) = -16.24 + 4.70 \alpha - \alpha \log(\nu_x/\nu_r) - (\alpha+1) \log B \quad (1)$$

where  $\nu_x$  is the observed X-ray frequency of  $2.4 \times 10^{17}$  Hz (1 keV),  $\nu_r$  is the observed radio frequency of  $1.4 \times 10^9$  Hz,  $\alpha$  is the spectral index of the (assumed) power law synchrotron spectrum ( $S_v \sim \nu^\alpha$ ), and  $B$  is the magnetic field strength in gauss. Application of this formula is complicated by the curvature of the Vir A radio spectrum, with spectral index ranging from  $\alpha = 0.9$  at 100 MHz to  $\alpha = 2.3$  at 10 GHz (Andernach et al. 1979). We must estimate the effective spectral index between the observed frequency 1.4 GHz and the frequency emitted by electrons responsible for the IC scattering of microwave photons to 1 keV. These electrons have Lorentz factors  $\gamma \sim (2 \times 10^{17} \text{ Hz} / 2 \times 10^{11} \text{ Hz}) \sim 1000$  and emit synchrotron around  $\nu \sim 80 (B/5 \mu\text{G})^2 (\gamma/1000) \text{ MHz}$ . Extrapolating the halo spectrum of Andernach et al. below 101 MHz, we obtain an effective spectral index between 1.4 GHz and 80 MHz of  $\alpha = 1.05$ . Using this value in equation (1) gives a predicted IC flux

$$\log(S_x/S_v) = -9.08 - 2.05 \log(B/5 \mu G) \quad (2)$$

The observed flux density ratio averaged over the entire halo is  $\log(S_x/S_v) = -7.96$  or 13 times this predicted level. It ranges between >6 and 70 times the predicted level at different location across the source (Table 1). This discrepancy is disturbing, but not conclusive, evidence against the IC model. The observed ratio  $S_x/S_v$  is unlikely to be low by more than a factor of 1.5 - 2. The conversion between HRI counts and flux density can only be ~50% higher than the value adopted in section IIa for any plausible power law plus absorption spectrum (Harris 1984). (The factor of 5 uncertainty in conversion factor mentioned in IIa applies only if a thermal spectrum is permitted.) The uncertainties in HRI counts rates or radio flux densities are probably below 20%. The discrepancy must therefore be associated with the predicted ratio in equations (1) and (2). The effective spectral index is accurate to  $\pm 0.1$ , and the constants in equation (1) are accurate to 20% (Harris and Grindlay 1979).

The only way to save the simple IC model is to invoke a magnetic field considerably below the average equipartition level of 5  $\mu G$ . An average level of 1.5  $\mu G$  across the halo and, at the east X-ray peak where  $\log(S_x/S_v)$  is highest, a level as low as 0.6  $\mu G$  is needed to get the observed high X-ray flux. The equipartition level of 4 - 6  $\mu G$  was estimated by Andernach et al. (1979) and Kotanyi (1980) from the overall properties of the halo. Although we do not have

localized spectral index maps or knowledge of the line-of-sight depths of the source at different locations, we can estimate the equipartition pressure in the west radio knot and southwest radio peak to be  $13 \mu\text{G}$ . (A flux density of 1 Jy at 1.4 GHz in a  $39'' \times 39''$  beam is observed; a  $39''$  line-of-sight depth and  $\alpha = 1.0$  is assumed.) The magnetic field must thus be  $\sim 30$  times below the equipartition level to account for the high X-ray flux at these locations.

#### (b) Thermal Emission

The principal alternative to the IC model is that the asymmetric X-ray component is due to thermal bremsstrahlung just like the symmetric component. Since thermal X-ray emissivity is strongly dependent on density and only weakly dependent on temperature, this requires a concentration of dense plasma at the locations of the X-ray structures east and southwest of the nucleus. Any local heating of ambient medium without simultaneous compression, due for instance to the leakage of relativistic electrons from the radio jets (e.g. Sofia 1973; Scott et al. 1980), is thus unlikely to account for the X-ray excess. The observed X-ray luminosity of  $4 \times 10^{41} \text{ ergs s}^{-1}$  is generated in a volume is  $\sim 5 \times 10^3 \text{ kpc}^3$ , assuming the line of sight depth of the region is similar to its north-south extent. The required density is then  $\sim 1 \times 10^{-2} \text{ cm}^{-3}$  for any reasonable temperature between  $5 \times 10^6$  and  $5 \times 10^7 \text{ }^\circ\text{K}$ . The external medium in the vicinity of the asymmetric component has density ranging from  $0.3 - 3 \times 10^{-4} \text{ cm}^{-3}$  and temperature around  $2 \times 10^7 \text{ }^\circ\text{K}$  (Stewart et al. 1984). Thus, if the asymmetrical emission is thermal its pressure

must exceed that of the ambient medium by one or two orders of magnitude. Assuming an equipartition magnetic field, it will exceed the internal pressure of the radio emitting region by a similar factor.

Given this substantial overpressure, the thermal model implies that the emission is transient. The gas will simultaneously cool due to line and bremsstrahlung emission, and expand into the surrounding gas on timescales of  $\sim 1 \times 10^9$  years. The exact balance between these processes depends on its unknown temperature; cooling will proceed faster than dissipation if the temperature is less than  $\sim 1 \times 10^7$  K. Though it is not self-evident whether this gas is entrained within the radio emitting region or lies outside of it, the latter possibility seems more likely. If entrained, the gas must be inhomogeneously distributed within the radio jets and would disrupt the field geometry due to its higher pressure. It would naturally occur outside the radio region if the jet's outward substantially exceeds the ambient sound speed of  $500 \text{ km s}^{-1}$ . The external medium would then be shocked and swept up by the jet much like a supernova remnant sweeps up the interstellar medium during its 'snowplow' phase. A major advantage of such a model is that precise spatial coincidence between the X-ray and radio emission is not expected. The fact that the X-ray component is brightest closer to the nucleus than the leading edges of the radio components may be due to the higher ambient gas density closer to the nucleus.

#### (c) Other Models

The third possible emission mechanism for the asymmetric X-ray component, synchrotron emission, can be readily discounted. The jet knots of Vir A and Cen A, where the X-rays are thought to be synchrotron, have flat radio spectra ( $\alpha = 0.6$ ) extending through the gigahertz band and (at least for Vir A) into the optical band. The Vir A halo has a rapidly steepening radio spectrum and no associated optical emission (Carter and Dixon 1978). Extrapolation of the radio spectrum into the X-ray band predicts flux densities orders of magnitudes below the observed levels.

Another possibility is that the X-ray emission has no relation to Vir A = M87, but is a chance superposition of a foreground or background object. Huchra and Brodie (1984) have found several galaxies within 3' of the center of M87 with redshifts of 25800 km/s. They appear to be members of a group or poor cluster 25 times more distant than the Virgo cluster. Huchra and Brodie suggest that the intracluster medium of this cluster may be responsible for the asymmetric X-ray emission, in which case its soft X-ray luminosity is  $\sim 2 \times 10^{44} \text{ erg s}^{-1}$ . We believe this explanation is improbable. First, this luminosity is very high, though not unprecedented, for poor clusters (Kriss et al. 1983). Such high luminosities only occur in cD-dominated poor clusters which have spherically symmetric X-ray distributions. Poor clusters with lumpy and asymmetric gas distributions generally have luminosities 2-4 orders of magnitude lower (e.g. Biermann et al. 1981). Second, this explanation does not account for the morphology of the X-ray structure (e.g., that the two arms are both pointed towards the nucleus of M87), nor for its

spatial association with the radio halo (e. g., that the position angles agree with the principal radio axes). There is no doubt that the radio halo is associated with M87, as it is far too bright and large to reside at the distance of the background cluster.

## V CONCLUSIONS

The principal observational results of this study are the HRI residual map (Figure 1b), the VLA 1.4 GHz map (Figure 2b), and their superposition (Figure 4). The asymmetrical X-ray emission and the radio halo are clearly associated with each other, but are not coincident. The ratio of X-ray to radio surface brightness ranges by a factor of 15, the structures differ in shape, and prominent radio features show no corresponding X-ray emission. Despite the quality of the observational material, the physical interpretation of the structures is not obvious. The radio halo clearly consists of energetic particles ejected from the nucleus. Its morphology is somewhat unusual, but it probably can be classified as a wide angle tail (WAT) source (Appendix B). The principal issue concerns the cause of the associated X-ray emission. If inverse Compton is the operative mechanism then the average magnetic field must be at least 10 times weaker than the equipartition or minimum energy value, and must vary considerably across the source. The alternative explanation is that the ejection of the radio emission plasma has caused local enhancement of thermal bremsstrahlung from the dense ambient medium. This should occur if the radio jet traveled outward at supersonic velocities, shocking and compressing the ambient

medium. The X-ray excess would persist for  $\sim 1 \times 10^9$  years before it cooled or dissipated.

We can envision two experiments that might distinguish between the inverse Compton and thermal models. The most definitive test would be an X-ray spectrum of the asymmetrical component. Spatial resolutions  $< 30''$  and spectral resolutions  $E/\Delta E > 100$  could determine whether the excess emission is a power law or is comprised of emission lines. This observation is well within the capability of the planned Advanced X-ray Astrophysics Facility and perhaps other missions. A less definitive test, though one which could be accomplished today, would be narrow band optical imagery around the H $\alpha$  line. This would determine whether cool gas is present in the vicinity of the east and southwest X-ray structures. Cool emission line filaments are known to exist in the densest gas within  $40''$  of the nucleus (Ford and Butcher 1979), but no detailed searches have been conducted in the halo region. While a negative result would not be informative, the detection of optical emission lines adjacent to the X-ray components would support a thermal model.

#### ACKNOWLEDGEMENTS

We would like to thank R. Perley for making available unpublished VLA data, Mr. M. Cline for his capable assistance with the radio analysis, and C. Lonsdale for his advice and software expertise. This work was principally supported by NASA grant NAG



8-357; additional support was provided by NSF grant 83-51447.

## Appendix A

### Eccentricity of the X-ray Emitting Gas

In their original analysis of the M87 HRI image, SGF reported that the X-ray surface brightness isophotes beyond the asymmetric component associated with the radio halo are approximately circular, in contrast to the considerable eccentricity of the optical isophotes in this region of M87. However, after the subtraction of the symmetric X-ray component described in section IIa above, large-scale regions of low surface brightness emission appeared along a northwest-southeast axis. It is best seen in Figure 1c as enhancements at the level of the lowest contour. V band photographic surface photometry of the stellar emission in M87 shows an eccentricity of about 10% around 1' from the nucleus increasing to about 40% around 3', and remaining at this high level beyond 30' (Carter and Dixon 1978). The orientation of the major axis is constant at P.A.  $155^\circ \pm 5^\circ$ , which is consistent with the X-ray enhancements. The X-ray excess appears in two regions, a  $\sim 8''$  diameter semicircle centered  $\sim 4'$  southeast of the nucleus, and a  $5' \times 10'$  region centered  $\sim 7'$  northwest of the nucleus. (Recall that  $10'$  corresponds to about 44 kpc.) The mean surface brightness is a few percent of the symmetric component, and the total luminosity of the regions is  $\sim 5 \times 10^{41} \text{ ergs s}^{-1}$ .

Ellipticity of X-ray isophotes in clusters of galaxies has not been widely discussed. Fabricant et al. (1984) have analyzed one case, Abell 2256, where the entire X-ray distribution (not just a few percent of the surface brightness) is elliptical with an axial ratio of 1.5 - 2.0 on scales of 3' to 30' (100 to 1000 kpc). The discovery of X-ray eccentricity in M87 is not surprising, as the X-ray gas must respond to the shape of the gravitational potential, which is presumably closely linked with the stellar distribution. A detailed analysis, which is outside the scope of this paper, of the X-ray and optical eccentricities might give insight into the distribution of non-luminous matter in that galaxy. The mass-to-luminosity ratio  $10'$  from the center of M87 is  $>50$ , as determined from the gravitational confinement of the symmetric X-ray gas (Fabricant and Gorenstein 1983), indicating that non-luminous mass dominates the gravitational potential at that radius. If the non-luminous mass has a less eccentric distribution than the stars, as may be suggested by the weak X-ray eccentricity, then a stellar origin of the non-luminous mass might be excluded.

#### Appendix B

##### Virgo A as a Radio Galaxy

We examine here the VLA maps of the radio halo (Figures 2a-c) not from the perspective of the associated X-ray emission, but as an improved view of an unusual radio galaxy. As described in section IIIa, the halo might be divided into four structures: (a) the knot 2.2' west of the nucleus; (b) the knot or lobe 3'-4' to the east; (c) the elongated component 2'-5' to the southwest; and (d) the large

scale envelope surrounding the entire source. We present here two rather different explanations of this structure, drawn from recent discussions of the origins of radio source morphologies.

One interpretation involves ejection of inhomogeneous opposing jets by a precessing nucleus. Models of this type have been proposed for radio galaxies and quasars possessing S-shaped symmetry (see Ekers 1982). If one includes the inner lobes of the 'core' component of Vir A, the the principal features of the source can be interpreted as three pairs of radio lobes ejected by a nucleus rotating counter clockwise. The first ejection was along the NE/SW axis and produced halo components (c) and (d) which, being oldest, extend furthest from the nucleus and are most diffuse. The second ejection produced the components (a) and (b) along a E/W axis. This third ejection is still in progress, and is responsible for the radio/optical/X-ray synchrotron jet and the inner lobes along an ESE/WNW axis. This explanation emphasizes the symmetries of the halo and would attribute asymmetries (e.g., components c and d are not equally luminous; components a and b are not equidistant from the nucleus) to interactions between the ejected material and ambient medium.

The second interpretation involves the continuous ejection of jets which bend or twist in various directions. Vir A is one of a number of radio galaxies (frequently cD giant ellipticals) at the center of rich clusters, and hence lie at rest in the center of a dense intracluster gas. The radio galaxies of these galaxies often show distorted structures that do not readily fit into standard

morphological classification schemes (classical doubles, head-tails, etc.). Examples of these central galaxies with radio extents similar to that of the Vir A halo ( $\sim 60$  kpc) include: 3C338 in Abell 2199, which has steep spectrum ridges and lobes (Burns et al. 1983); Per A = 3C84 in the Perseus cluster, which has an amorphous low surface brightness outer lobe surrounding a bright core and jet (Gisler and Miley 1979); and 3C318.1 in MKW 3S, which has only one lobe with a very steep spectrum (Fomalont et al. in preparation). Though each is unique in detail, they have been generally classified as wide angle tail sources (WATs) characterized by ejecta that travel slowly outward from the central galaxy, bending and twisting in unpredictable directions (Burns 1983). Their morphologies might be determined by buoyancy forces, motions or inhomogeneities in the external medium, or electric currents traveling along their jets. If Vir A were in a distant cluster of galaxies and only a low resolution map like Figure 2a were available, it probably would be classified as a WAT with two distorted jets. The twisting jet model is supported by the apparent continuity of the surface brightness and the magnetic field orientation in Figures 2b and 3 that suggest a direct connection between the west knot (component a) and the southwest jet (component c). Such a connection would not be expected in the precessing nucleus model.

Elucidation of the source physics in Vir A would benefit from high quality spectral index maps and a detailed multi-frequency polarization study to unravel the complex mixture of intrinsic polarized emission and foreground Faraday effects that are likely to

be present. While such data are not yet available, the polarization map shown in Figure 2c is very intriguing in this regard. The southwest component is strongly polarized, with polarization fractions up to 28%, while the eastern component is totally unpolarized, with an average polarization  $<0.8\%$  (3 sigma limit). This polarization distribution is consistent with that found by Seielstad and Weiler (1969) in a one-dimensional scan and by Andernach et al. (1979), but differs from that of Kotanyi (1980). Andernach et al. report a polarization fraction of  $21 \pm 5\%$  for the south-west component at 4.8 GHz, with the peak polarization intensity appearing  $\sim 3'$  to the southwest of the peak total intensity. Kotanyi finds a peak polarization of 6 % for the east component at 610 MHz and significant polarized flux from the vicinity of the western knot (our component a), but little polarized from the southwest region. It is not clear whether these differences are instrumental in origin, result from different beam widths, or are intrinsic to the source.

The reason for the startling difference in polarization fraction between the east and southwest sides of the halo in our 1.4 GHz map is not self-evident. Perhaps the eastern component have detailed polarization substructure that is blurred by the 39" beam. Alternatively, it may be oriented away from us so that its radiation must pass through the dense gaseous core, subjecting its polarized flux to many small scale rotations that randomize the polarization angles. The southwestern structure would then be directed towards us and suffer less Faraday rotation. The apparent homogeneity of its field structure in Figures 2a and 2b suggests that there is not much

differential Faraday rotation across the component. Comparison of the position angle P.A.  $\sim 100^\circ - 160^\circ$  of the polarized flux in our 1.4 GHz map (which is consistent with the  $147^\circ \pm 14^\circ$  angle found by Seielstad and Weiler [1969]) with the higher frequency polarization orientations reported by Andernach et al. (1979) indicates that considerable Faraday rotation is present. We believe it is premature to estimate the effect quantitatively, given the complex structure and incompatible beam sizes.

Table 1

Radio and X-ray Surface Brightness at  
Selected Locations in the Halo

Region	$S_{1.4}$ (Jy)	Polar. (%)	HRI cts/beam	$S_x$ ( $\mu$ Jy)	$\log(S_x/S_{1.4})$	$\alpha_{rx}$
1. North radio halo	0.27	<3	<24	<0.005	<-7.72	>-0.94
2. East radio peak and X-ray spot	1.00	<1	81	0.017	-7.76	-0.94
3. East X-ray peak	0.65	<1	168	0.036	-7.26	-0.88
4. Southeast X-ray bridge	0.36	1	75	0.016	-7.35	-0.89
5. West radio knot	1.07	1	<24	<0.005	<-8.31	>-1.01
6. Southwest X-ray peak	0.68	6	121	0.026	-7.42	-0.90
7. Southwest radio peak	1.00	5	44	0.009	-8.03	-0.97
8. Southwest radio polarization peak	0.55	28	24	0.005	-8.02	-0.97



## References

- Andernach, H., Baker J. R., von Kap-Herr, A. and Wielbinski, R.  
1979, *Astr. Astrophys.* 74, 93.
- Baars, J. W., Genzel, R., Pauliny-Toth, I. I., and Witzel, A. 1977,  
*Astr. Astrophys.* 61, 99.
- Biermann, P., Kronberg, P., and Madore, B. F. 1982, *Ap. J. Letters*  
256, L37.
- Bridle, A. H. 1984, *Astron. J.* 89, 979.
- Burns, J. O. in *Astrophysical Jets* (A. Ferrari and A. G.  
Pacholczyk eds.) Dordrecht:Reidel, p. 67.
- Burns, J. O., Feigelson, E. D. and Schreier, E. J. 1983, *Astrophys.*  
*J.* 273, 128.
- Burns, J. O., Nelson, E. R., White, R. A., and Gregory, S. A. 1985  
*Astrophys. J.* 291, 611.
- Burns, J. O., Schwendeman, E., and White, R. A. 1983, *Ap. J.* 271,  
575.
- Cameron, M. J. 1971, *M.N.R.A.S.* 152, 439.
- Carter, D. and Dixon, K. L. 1978. *Astron. J.* 83, 578.
- Cooke, B. A., Lawrence, A., and Perola, G. C. 1978, *M.N.R.A.S.*  
182, 661.
- Dennison, B. 1980, *Astrophys. J.* 236, 761.
- Ekers, R. D. 1982, in *Extragalactic Radio Sources* (D. S. Heeschen  
and C. M. Wade, eds.) Dordrecht:Reidel, p. 465.
- Fabricant, D., Lecar, M., and Gorenstein P. 1980, *Astrophys. J.*  
241, 552.

- Fabriziant, D. and Gorenstein, P. 1983, *Astrophys. J.* 267, 535.
- Fabriziant, D., Rybicki, G., and Gorenstein, P. 1984, *Astrophys. J.* 286, 186.
- Feigelson, E. D. 1983, in *Astrophysical Jets* (A. Ferrari and A. G. Pacholczyk, eds.) Dordrecht: Reidel, p. 165.
- Feigelson, E. D. 1985, in *Compact Galactic and Extragalactic X-ray Sources* (Y. Tanaka and W. H. Lewin, eds.), p.
- Feigelson, E. D. and Berg, C. J. 1983, 269, 400.
- Feigelson, E. D., Schreier, E. J., Delvaille, J. P., Giacconi, R., Grindlay, J., and Lightman, A. P. 1981, *Astrophys. J.* 251, 31.
- Ford, H. C. and Butcher, H. 1979, *Ap. J. Suppl.* 41, 147.
- Giacconi, R. et al. *Astrophys. J.* 230, 540.
- Gisler, G. R. and Miley, G. K. 1979, *Astr. Astrophys.* 76, 109.
- Harris, D. E. (ed.) *Einstein Observatory Revised User's Manual*, 1984, Harvard-Smithsonian Center for Astrophysics.
- Harris, D. E. and Grindlay, J. E. 1979, *M.N.R.A.S.* 188, 125.
- Harris, D. E., Costain, C. H. and Dewdney, P. E. 1984, *Astrophys. J.* 280, 532.
- Huchra, J. and Brodie, J. 1984, *Astrophys. J.* 280, 547.
- Kotanyi, C. 1980, *Astr. Astrophys.* 83, 245.
- Kriss, G. A., Cioffi, D. F., and Canizares, C. R. 1983, *Astrophys. J.* 272, 439.
- Marshall, F. J. and Clark, G. W. 1981, *Astrophys. J.* 245, 840.
- Miley, G. 1980, *Ann. Rev. Astron. Astrophys.* 18, 165.
- Mills, B. Y. 1952, *Nature* 170, 1063.
- Reid, M. J., Schmitt, J. H., Owen, F. N., Booth, R. S., Wilkinson,

- P. N., Shaffer, D. B., Johnston, K. J., and Hardee, P. E.  
1982, *Astrophys. J.* 263, 615.
- Schreier, E. J., Gorenstein, P. and Feigelson, E. D. 1982,  
*Astrophys. J.* 261, 42. (SGF)
- Scott, J. S., Holman, G. D., Ionson, J. A. and Papadopoulos,  
K. 1980, *Ap. J.* 239, 739.
- Seielstad, G. A. and Weiler, K. W. 1969, *Astrophys. J. Suppl.*  
18, 85.
- Sofia, S. 1973, *Ap. J. Letters* 179, L31.
- Sramek, R. A. 1982, in *Synthesis Mapping* (A. R. Thompson and L.  
R. D'Addario, eds.), *Proc. NRAO-VLA Workshop*, p. 2-1.
- Stewart, G. C., Canizares, C. R., Fabian, A. C., and Nulsen,  
P. E. 1984, *Astrophys. J.* 278, 536.
- Thompson, A. R., Clark, B. G., Wade, C. M., and Napier, P. J.  
1980, *Astrophys. J. Suppl.* 44, 151.
- Turland, B. D. 1975, *M.N.R.A.S.* 170, 281.
- Willingale, R. 1981, *M.N.R.A.S.* 194, 56.

## Figure Captions

Figure 1. Einstein HRI map of Vir A = M87: (a) the original image smoothed with a 15" FWHM Gaussian (contour levels 1, 2, 3, 4, 6, 8, 10, 15, 20, 50, and 90% of the peak 220 HRI counts/beam); (b) the residual emission after subtraction of the symmetrical component, smoothed to 15" FWHM (contour levels -0.75, 0.75, 1.5, 2.5, 3.5, 5, 15, 50, 90% of the peak 218 HRI counts/beam); and (c) the same residual map smoothed to 39" FWHM for comparison with the radio maps (contour levels -1, 1, 2, 3, 4, 6, 10, 50, and 90% of the peak  $2.61 \times 10^3$  HRI counts/beam).

Figure 2. VLA 1.4 GHz map of Vir A = M87: (a) tapered map with 72" FWHM synthesized beam (contour levels -0.2, 0.2, 0.5, 1.0, 1.5, 2.0, 2.5, 5, 10, 20, 30, 50, 70, and 90% of the peak 108 Jy/beam; polarization vector length 1' corresponds to 0.19 Jy/beam); and (b) untapered map with 39" FWHM beam (contour levels -0.1, 0.1, 0.3, 0.3, 0.6, 0.9, 1.2, 1.5, 5, 20, 50, and 90% of the peak 72.4 Jy/beam; polarization vector length 1' corresponds to 0.15 Jy/beam).

Figure 3. VLA 5 GHz map of Vir A = M87, tapered with 40" FWHM synthesized beam (contour levels -0.2, -0.1, 0.1, 0.2, 0.3, 1, 5, 20, 50, and 90% of the peak 42.5 Jy/beam).

Figure 4. Superposition of selected contours of the 39" resolution radio (solid lines) and X-ray (dashed lines) maps, with the eight

locations listed in Table 1 marked.

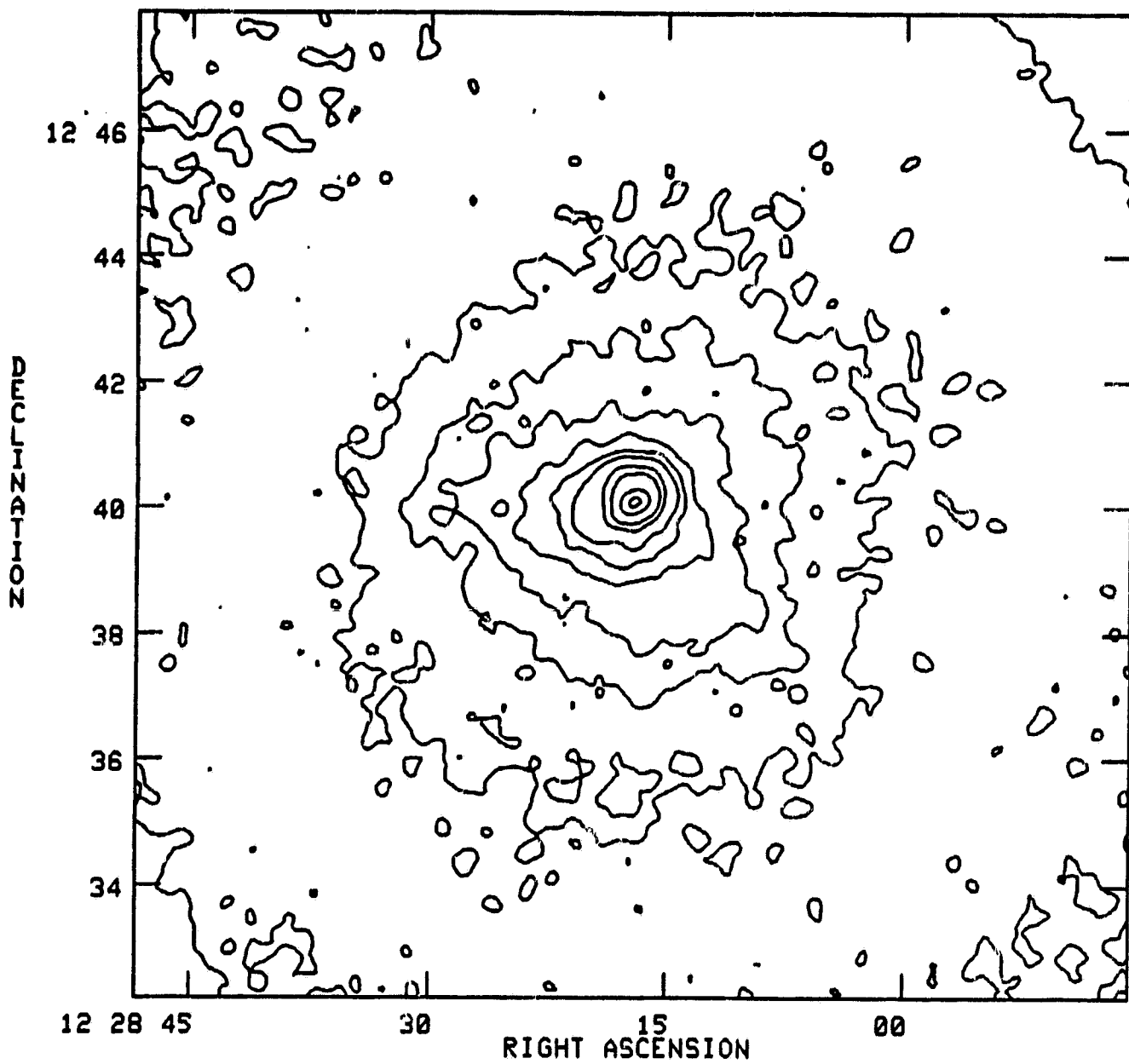


Fig 1a

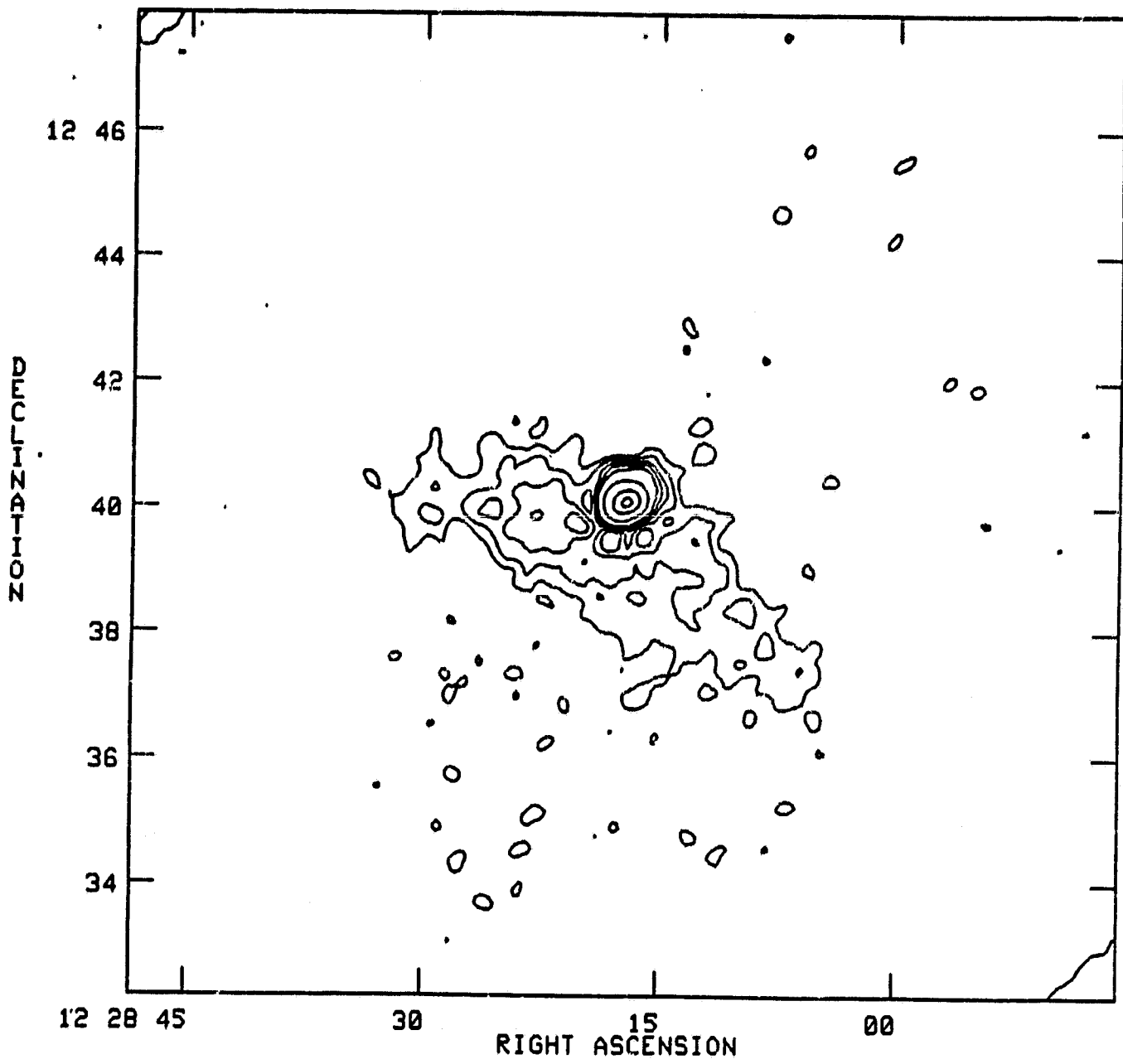


Fig. 1b

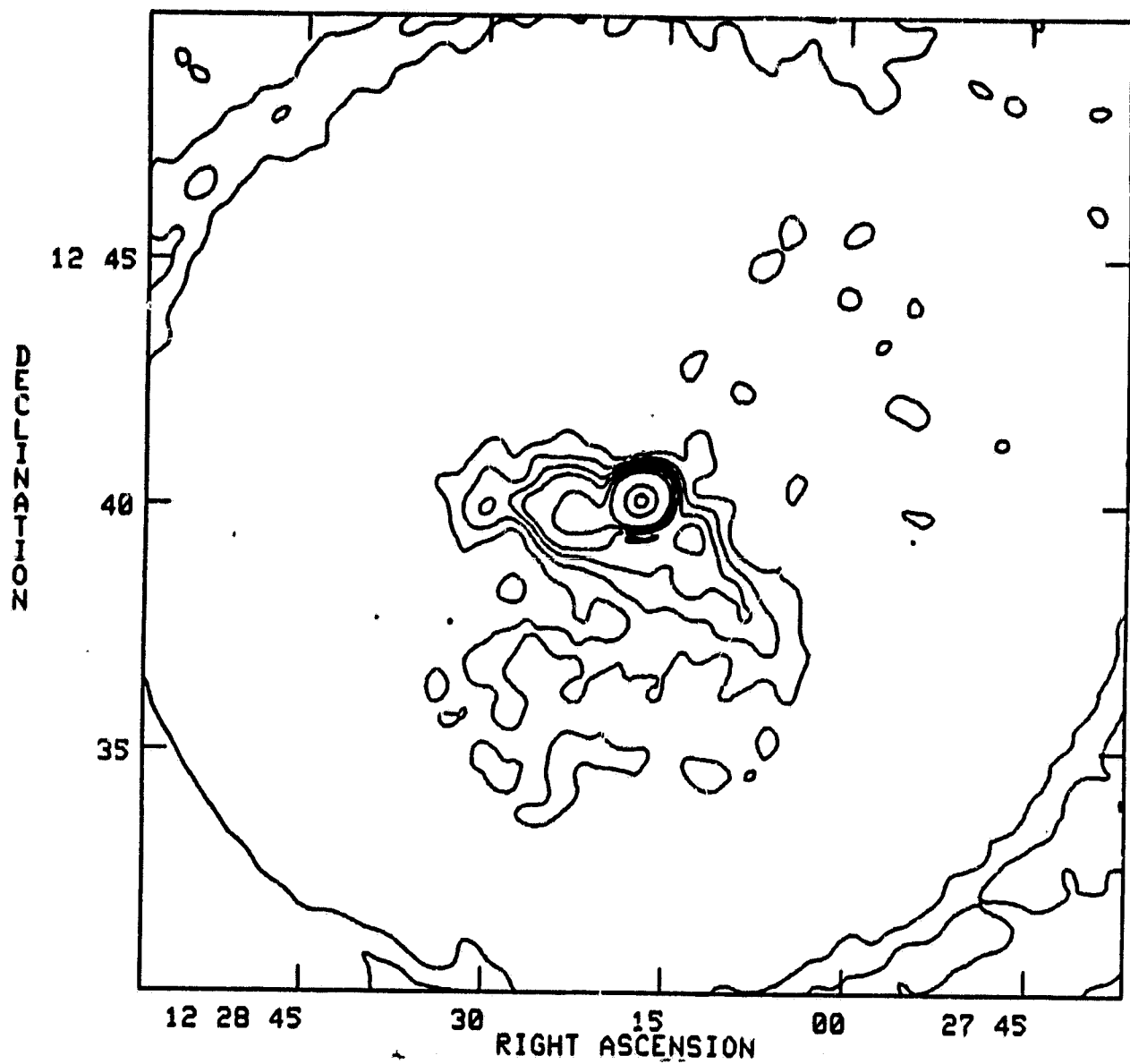


Fig 1c



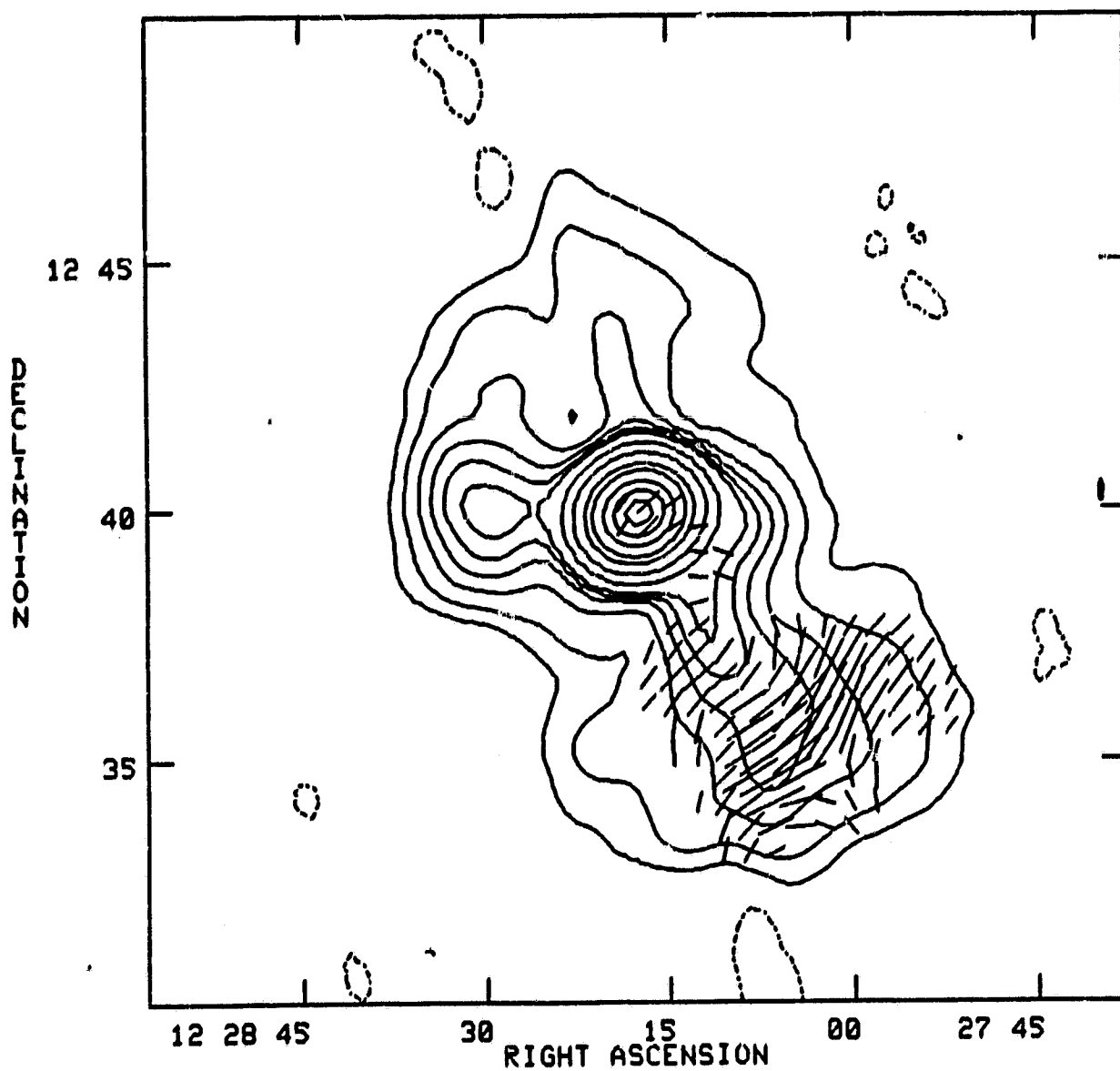


Fig 2a

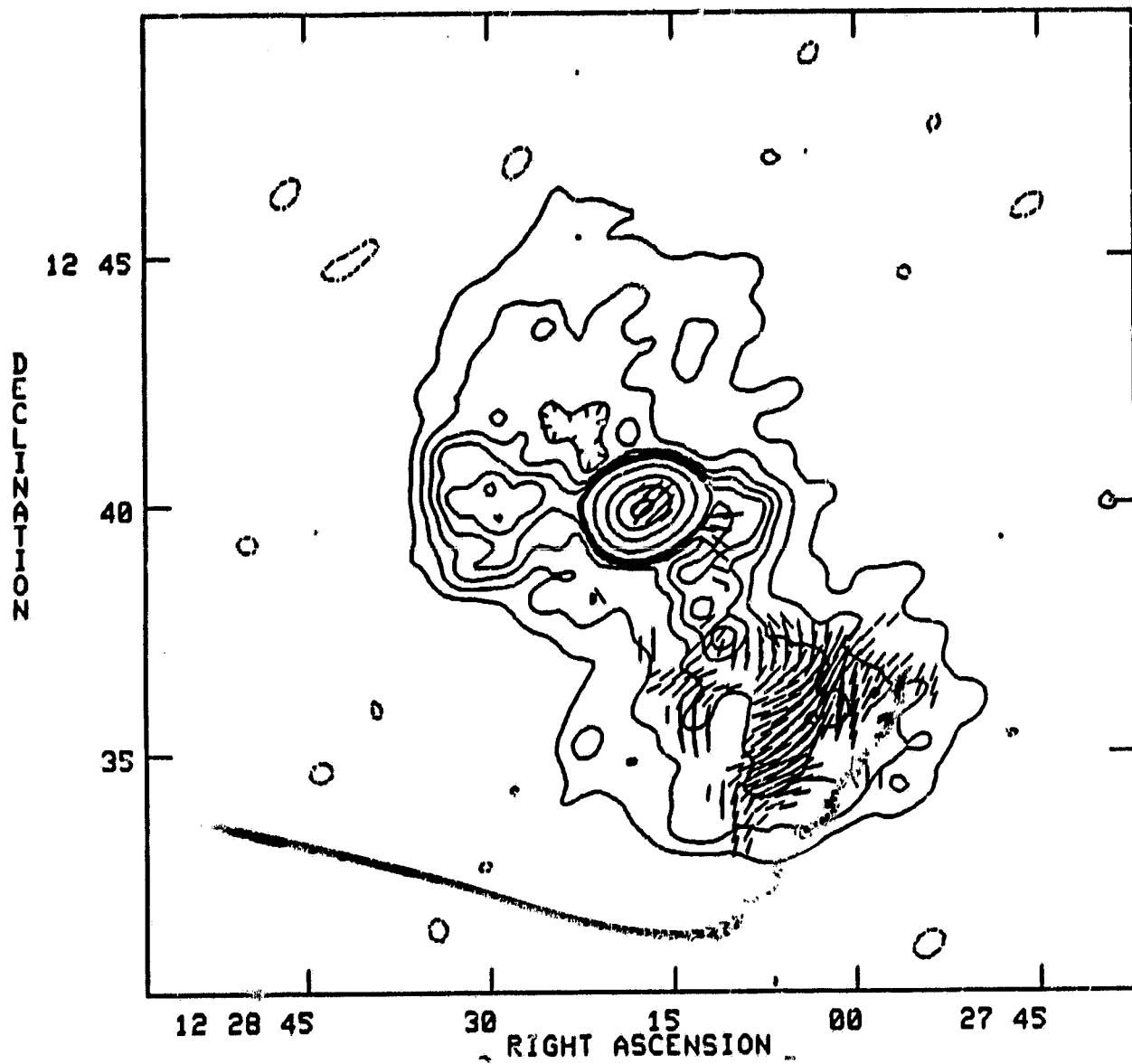


Fig 2b

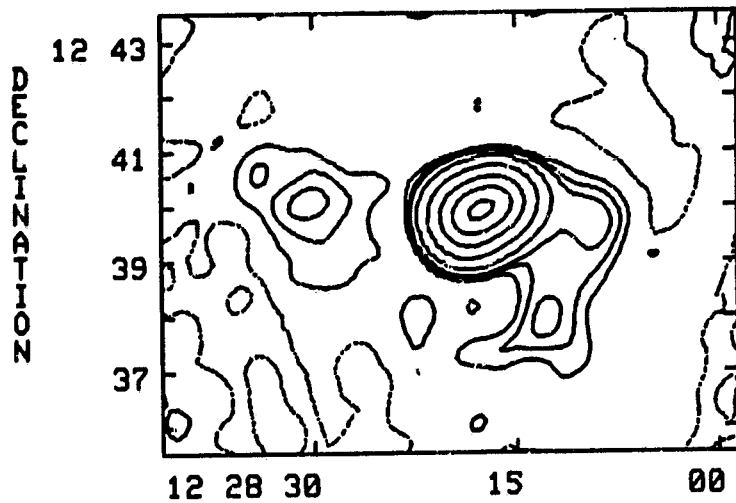


Fig 3

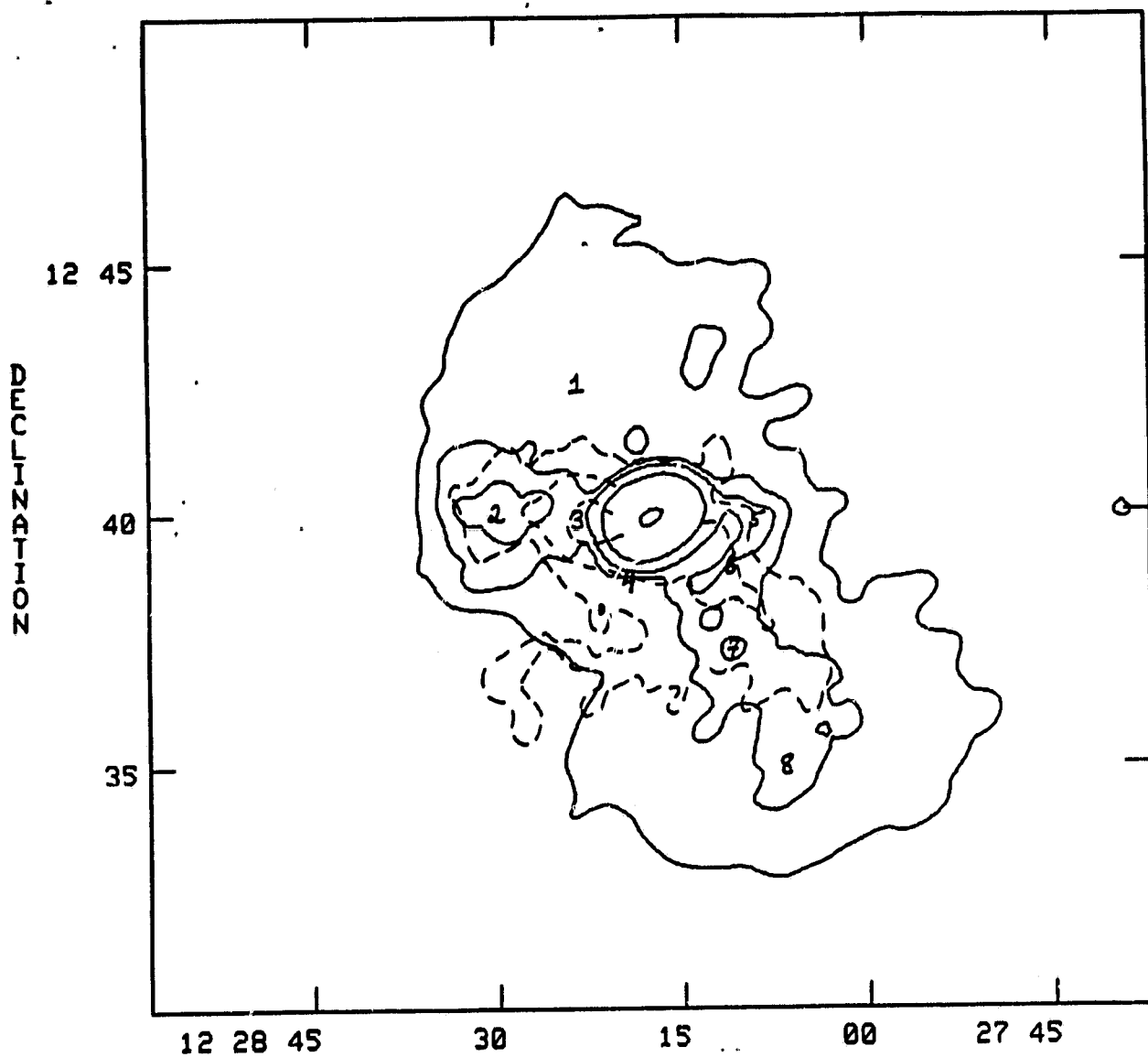


Fig 4